

1 **Thermal equation of state of the main minerals of eclogite: Constraining the**
2 **density evolution of eclogite during delamination process in Tibet**

3 Zhilin Ye ^{a,b}, Dawei Fan ^{a,*}, Bo Li ^c, Qizhe Tang ^d, Jingui Xu ^{e,*}, Dongzhou Zhang ^e, Wenge Zhou ^a

4 ^a *Key Laboratory of High-Temperature and High-Pressure Study of the Earth's Interior, Institute of*
5 *Geochemistry, Chinese Academy of Sciences, Guiyang, Guizhou 550081, China*

6 ^b *University of Chinese Academy of Sciences, Beijing 100049, China*

7 ^c *Research Institute of Petroleum Exploration & Development-Northwest (NWGI), PetroChina Lanzhou*
8 *730020, China*

9 ^d *School of Information Engineering, Huzhou University, Huzhou, Zhejiang 313000, China*

10 ^e *Hawaii Institute of Geophysics and Planetology, School of Ocean and Earth Science and Technology,*
11 *University of Hawaii at Manoa, Honolulu, Hawaii 96822, USA*

12 * Corresponding authors:

13 *E-mail addresses:* fandawei@vip.gyig.ac.cn (D. Fan), xujingui@hawaii.edu (J. Xu)

14

15 **Abstract**

16 Tibet, which is characterized by collisional orogens, has undergone the process of delamination or
17 convective removal. The lower crust and mantle lithosphere appear to have been removed through
18 delamination during orogenic development. Numerical and analog experiments demonstrate that
19 the metamorphic eclogitized oceanic subduction slab or lower crust may promote gravitational
20 instability due to its increased density. The eclogitized oceanic subduction slab or crustal root is
21 believed to be denser than the underlying mantle and tends to sink. However, the density of
22 eclogite under high-pressure and high-temperature conditions and density differences from the

23 surrounding mantle is not precisely constrained. Here, we offer new insights into the derivation
24 of eclogite density with a single experiment to constrain delamination in Tibet. Using *in situ*
25 synchrotron X-ray diffraction combined with diamond anvil cell, experiments focused on minerals
26 (garnet, omphacite, and epidote) of eclogite are conducted under simultaneous high-pressure and
27 high-temperature conditions, which avoids systematic errors. Fitting the pressure-temperature-
28 volume data with the third-order Birch-Murnaghan equation of state, the thermal equation of state
29 (EoS) parameters, including the bulk modulus (K_{T0}), its pressure derivative (K_{T0}'), and the thermal
30 expansion coefficient (α_0), are derived. The densities of rock-forming minerals and eclogite are
31 modeled along with the geotherms of two types of delamination. The delamination processes of
32 subduction slab breakoff and the removal of the eclogitized lower crust in Tibet are discussed. The
33 Tibetan eclogite which containing 40-60 vol. % garnet and 44-70% degrees of eclogitization can
34 promote the delamination of slab break-off in Tibet. Our results indicate that eclogite is a major
35 controlling factor in the initiation of delamination. A high abundance of garnet, a high Fe-content,
36 and a high degree of eclogitization are more conducive to instigating the delamination.

37 **Keywords:**

38 Eclogite, Equation of state, Single-crystal X-ray diffraction, Delamination, Tibet

39

40 **1. Introduction**

41 The evolution of orogenesis is characterized by lithospheric removal during rapid surface uplift,
42 mantle upwelling, and postcollisional magmatism, particularly in the Central Andes (e.g. Ehlers
43 and Poulsen, 2009), Himalayas (e.g. Singh and Kumar, 2009), and Dabie orogen (e.g. He et al.,
44 2011).

45 It is widely accepted that delamination is the most important mechanism of lithospheric
46 removal. Delamination is induced and accompanied by two major requisites: (a) the density
47 difference caused by the negative buoyancy of the delaminated lithosphere; and (b) the presence
48 of a weak lower crust (lower viscosity) that exists between the strong upper crust and lithospheric
49 mantle. Usually, two types of delamination are believed to occur in orogen development. The first
50 is the conventional definition of delamination proposed by Bird (1978, 1979), which was used to
51 interpret the geodynamic evolution of the Colorado Plateau. In this scenario, mantle lithosphere
52 peels back from the overlying upper crust and is removed entirely, with the rising hot mantle
53 filling the lithospheric removal zone (e.g. Göğüş and Ueda, 2018; Krystopowicz and Currie, 2013).
54 A weak decoupling layer, i.e, the lower crust, is an essential condition in this delamination model,
55 which may be affected by the rheological behavior of the hydration, thermal, and chemical
56 characteristics of the lithosphere (e.g. Morency, 2004). In addition to conventional delamination,
57 an alternative delamination mechanism is convective removal based on the Rayleigh-Taylor-type
58 instability model (Houseman et al., 1981), namely, viscous “dripping”. This model postulates that
59 there is sufficient perturbation in the lithospheric mantle, which is ascribed to the strong
60 temperature-dependence of typical mantle rheology, without regard to a specific weak layer (e.g.
61 Conrad and Molnar, 1999; Houseman and McKenzie, 1982).
62 All previous studies attribute the gravitational instability process of lithospheric removal to the
63 negative thermal buoyancy of the cold lithosphere (Conrad and Molnar, 1999; Houseman and
64 McKenzie, 1982) or density contrast between asthenosphere and mantle lithosphere. In any case,
65 the density distribution with lithosphere pressure and temperature (*P-T*) conditions and chemical
66 composition is of vital importance to understanding the process of lithospheric removal.

67 The Tibetan Plateau is the most representative and prominent collisional orogens. Two types of
68 delamination are proposed to proceed (e.g. Chung et al., 2005; Houseman et al., 1981):
69 lithospheric mantle removal and thickened eclogitized crust removal. The Neo-Tethyan oceanic
70 subduction, India-Asia collision, and Indian continental subduction could be further considered
71 responsible for the abnormal thinning of the mantle lithosphere under Tibet (Chung et al., 2005; Li
72 et al., 2019). The lithospheric removal event in Tibet corresponds to Neo-Tethyan oceanic slab
73 break-off. The mechanism is primarily based on density contrasts between the denser mantle
74 lithosphere and the lighter underlying mantle. Some models reveal that lithospheric removal is
75 induced by the retreating high-density eclogitized lithosphere detached from overlying low-
76 density crust (Faccenda et al., 2009; Li et al., 2016). Other alternative models indicate that
77 thickened eclogitized crust is a potential factor deriving lithospheric removal because the
78 eclogitized crustal root is denser than the underlying mantle and tends to sink (Krystopowicz and
79 Currie, 2013). Regardless of the above types of delamination, the density of eclogite is closely
80 related to delamination. Therefore, Tibet provides an excellent opportunity to understand the role
81 of eclogite density in the process of delamination.

82 An immense amount of concrete research has focused on the origin and appearance of
83 lithospheric mantle removal from different angles, such as geophysical (Ren and Shen, 2008),
84 geological (Chung et al., 2005), petrological (Chung et al., 2005; Turner et al., 1993), numerical
85 and analog experiments (Göğüş and Pysklywec, 2008; Morency, 2004). In particular, numerical
86 and analog experiments are used as prominent methods to simulate the dynamics of delamination
87 (Göğüş and Ueda, 2018). Of these studies, the density behavior occurring during the delamination
88 process has also been investigated intensively following thermodynamic (Semprich et al., 2010),

89 seismic/tomography (Matchette-Downes et al., 2019), and numerical simulations (Li et al., 2016).
90 However, few studies have systematically illuminated the issue of delamination from the
91 perspective of eclogite density. Here, we attempt to offer new insights into the derivation of rock
92 density through the mineral physics method to constrain delamination in Tibet (Ye et al., 2021).
93 Conducting a single experiment under high-pressure and high-temperature conditions, we obtain
94 the equation of state (EoS) of the main minerals of eclogite with fewer systematic errors in the
95 experiment. Furthermore, the newly derived EoS of the main minerals of eclogite, combined with
96 the published EoSs of the main minerals of peridotite (Ye et al., 2021), geothermal lines, and
97 collected eclogite mineral compositions, are further used to elucidate a density evolution model
98 during the delamination process in Tibet. We argue that the EoSs of minerals could be used in a
99 straightforward manner as new constraints on the construction of the density model. Using a
100 simplistic calculation setup, in this study, this density evolution model will shed light on the
101 possibility of delamination during the orogen process.

102

103 **2. Geological background**

104 The Tibetan Plateau is composed of four terranes from south to north: the Himalaya, Lhasa,
105 Qiangtang, and Songpan-Ganzi terranes (Fig. 1). The birth of the Himalayas and Tibetan Plateau
106 is a consequence of the Indo-Asian collision, which began in the early Cenozoic (Hodges et al.,
107 2001; Wang et al., 2008). The Neo-Tethyan oceanic slab is proposed to have detached from the
108 Indian lithosphere, and the onset of the Indo-Asian collision (DeCelles et al., 2002) particularly
109 occurred in the lower part of the Indian and Lhasa lithospheres. The tectonic evolutionary history
110 of the Lhasa terrane and Tethys Himalayas is essential for revealing the origin of the Himalayan-

111 Tibetan orogen. The subducting Neo-Tethyan slab was thrust into southern Tibet approximately
112 70-65 Ma (Fig. 1b). With the closure of the Neo Tethyan Ocean, the India-Asia continent collision
113 caused compressional deformation in southern Tibet, and a series of collision breakoff events were
114 delineated spanning from 65 Ma to 42 Ma (Chung et al., 2005, 2009; Ma et al., 2014; Zhu et al.,
115 2015). During this period, the Indian continental lithosphere might have dragged down to deeper
116 depths during subduction. Meanwhile, slab rollback accompanied by the southward migration of
117 asthenospheric convection in Tibet changed the thermal structure of the mantle wedge. The
118 breakoff of the oceanic Neo-Tethyan slab from the more buoyant Indian continental lithosphere
119 indicated by the eruption of early Eocene Linzizong volcanic rocks in the Gangdese arc or the
120 cessation of Gangdese arc magmatism occurred at ~45 Ma (DeCelles et al., 2002), which opened a
121 channel for the upwelling asthenosphere (Chung et al., 2009; Ma et al., 2014; Zhu et al., 2015).
122 Additionally, geophysical evidence of longitudinal wave (V_P) tomography is interpreted for the
123 north-dipping high-speed anomaly, which is ascribed to the deep Indian mantle lithosphere (Li et
124 al., 2008). Subsequently, the subduction of the Indian continental margin continues at a low
125 subduction angle beneath the Lhasa terrane (Guillot et al., 2008).

126 In addition, 25 Ma to 0 Ma is another period considered to contain either the occurrence of slab
127 breakoff (Miller et al., 1999) or lithospheric mantle removal following slab breakoff (Chung et al.,
128 2005; Nomade et al., 2004). Previous studies suggested that the hotter asthenosphere considerably
129 raised the geothermal conditions during this period (Chung et al., 2005). Magmatism of the
130 ultrapotassic, shoshonitic, and calc-alkaline was widespread, which was potentially due to the
131 partial melts of the metasomatized lithospheric mantle and eclogitized lower crust. An adopted
132 model of convective lithospheric removal below Lhasa is widely followed (Miller et al., 1999).

133 The lithospheric removal-related mantle upwelling process has been supported by geological,
134 geophysical, and petrological studies (Chung et al., 2005; Ren and Shen, 2008; Turner et al., 1993).

135 Here, slab breakoff and convective lithospheric removal under Tibet are adopted as the
136 background in this study to discuss the possibility of the delamination process.

137

138 **3. Materials and methods**

139 **3.1 Starting material**

140 Natural garnet, omphacite, and epidote samples are collected from eclogite in the Dabie-Sulu
141 [ultra-high pressure metamorphic](#) (UHPM) belt. The compositions of each mineral are determined
142 to be $\text{Prp}_{21}\text{Alm}_{47}\text{Grs}_{31}\text{Sps}_{1}$ (Prp = pyrope, Alm = almandine, Grs = grossular, and Sps =
143 spessartine) for garnet, $\text{Quad}_{48}\text{Jd}_{45}\text{Ae}_{7}$ (Quad = Ferrosilite + enstatite + wollastonite, Jd = jadeite,
144 Ae = aegirine) for omphacite, and $\text{Ca}_{2.02}\text{Fe}_{0.75}\text{Al}_{2.32}\text{Si}_{0.16}[\text{SiO}_4][\text{Si}_2\text{O}_7]\text{O(OH)}$ for epidote. The

145 compositions of garnet and omphacite are shown in Figure 2 and are within the range of natural
146 mineral compositions of eclogite from Tibet. The chemical composition of representative epidote
147 minerals in Tibet shows that the Fe content of epidote exposed in eclogite is in the range of 0.13-
148 0.25 ($X_{\text{Fe}} = \text{Fe}^{3+}/(\text{Fe}^{3+} + \text{Al}^{3+})$) (Huang et al., 2015; Li et al., 2017; Liu et al., 2016), while the Fe
149 content of epidote in this study is 0.24, which is within the Fe content range of natural epidote.

150 The samples used in this study are representative of garnet, omphacite, and epidote minerals in
151 natural eclogites from Tibet. The garnet, omphacite, and epidote with high-quality grains are
152 separated from the eclogite specimens. The above three samples are crushed into $30 \times 40 \mu\text{m}^2$ chips
153 with a single crystal thickness of $15 \mu\text{m}$ in our experiment.

154 **3.2 Synchrotron X-ray diffraction**

155 The high-pressure and high-temperature experiment is conducted by a BX90 externally-heated
156 diamond anvil cell (EHDAC) with $\pm 15^\circ$ opening angles. The above three single crystals are
157 loaded into the BX90 EHDAC equipped with a pair of 500 μm culet-size diamond anvils and
158 tungsten carbide (WC) seats (Figure S1). The rhenium (Re) gasket is pre-indented to a thickness
159 of $\sim 60 \mu\text{m}$, and a cylindrical hole with a diameter of 360 μm is drilled as a sample chamber. Gold
160 powder is also loaded as the pressure calibrant (Fei et al., 2007), and neon is loaded as the
161 pressure transmitting medium through the GeoSoilEnviroCARS (GSECARS) gas loading system
162 (Rivers et al., 2008). The quasi-hydrostatic condition in the sample chamber can be maintained up
163 to $\sim 20 \text{ GPa}$ using the neon pressure transmitting medium (Finkelstein et al., 2017). On the other
164 hand, high temperature can significantly decrease the deviatoric stress conditions in the sample
165 chamber. Moreover, previous studies demonstrate that the deviatoric stress disappears at the
166 temperatures of 650 K with neon as the pressure transmitting medium (Klotz et al., 2009; Meng et
167 al., 1993). Therefore, the hydrostatic/quasi-hydrostatic conditions can be maintained within the P -
168 T range of our experiment ($\sim 700 \text{ K}$, 25 GPa). An automated pressure-driven membrane system is
169 utilized to generate increasing pressure up to 25.6 GPa. High-temperature conditions up to 700 K
170 are provided by the heating resistor. Before collecting data, the temperature in the sample chamber
171 will be stabilized for 5 minutes and the temperature fluctuation is less than 1 K. Setup details for
172 the employed thermocouples and heaters can be found in our previous articles (Xu et al., 2019,
173 2020b; Ye et al., 2021).

174 *In-situ* synchrotron single-crystal X-ray diffraction (XRD) experiments were performed at
175 experimental station 13-BM-C of the Advanced Photon Source, Argonne National Laboratory. The
176 detailed experimental process and associated parameters can be seen in our previous studies (Xu et

177 al., 2017, 2018, 2020a; Zhang et al., 2017a). The diffraction images and the lattice parameters
 178 were analyzed by the Bruker APEX3 software package (Dera et al., 2013). The representative
 179 single-crystal X-ray diffraction patterns are shown in Figure S2. The specific unit-cell parameters
 180 of the above three samples at each P - T condition can be found in Table S1.

181

182 **4 Results and discussions**

183 **4.1 EoS of main minerals for eclogite**

184 The pressure-volume-temperature (P - V - T) data in this study are fitted by the third-order Birch-
 185 Murnaghan-EoS (BM3-EoS) (Birch, 1947) **in combination with the Holland-Powell thermal-**
 186 **pressure EoS (Holland and Powell, 2011)** to obtain the thermal EoS parameters. The volume is
 187 calculated in P - T space starting with an isothermal compression and followed by a path along an
 188 isochor curve to the final temperature. The pressure at a given volume and temperature consists of
 189 the following two parts:

190
$$P(V, T) = P(V, T_0) + P_{\text{th}}(V, T) \quad (1)$$

191 The first term corresponds to the pressure calculated by the BM3-EoS for compression at room
 192 temperature (T_0). The zero-pressure volume (V_{T0}), the isothermal bulk modulus (K_{T0}), and its
 193 pressure derivate (K_{T0}') with the following form:

194
$$P(V, T_0) = (3/2) K_{T0} \left[\left(V_{T0} / V \right)^{7/3} - \left(V_{T0} / V \right)^{5/3} \right] \times \left\{ 1 + (3/4) (K_{T0}' - 4) \left[\left(V_{T0} / V \right)^{2/3} - 1 \right] \right\} \quad (2)$$

196 The second term is the additional pressure generated by heating along an isochor. The thermal-
 197 pressure is following the equation:

198
$$P_{\text{th}}(V, T) = \alpha_{V,0} K_{T0} \left(\frac{\theta_E}{\xi_0} \right) \left(\frac{1}{\exp(\theta_E / T) - 1} - \frac{1}{\exp(\theta_E / T_0) - 1} \right) \quad (3)$$

199 where $\xi = \frac{(\theta_E/T)^2 \exp(\theta_E/T)}{((\theta_E/T)-1)^2}$, ξ_0 is the value of ξ at the reference temperature T_0 and α_{V0} is

200 the thermal expansion coefficient at room temperature. The Einstein temperature θ_E in this study
201 are selected and recalculated from the literature (Faccincani et al., 2021; Gottschalk, 2004).

202 The thermal EoS parameters are derived using the EoSFit program at high-pressure and room-
203 temperature and high-pressure and high-temperature conditions (Angel et al., 2014) and are shown
204 in Table S2. Under ambient pressure and temperature conditions, the measured V_0 values of garnet,
205 omphacite, and epidote are 1566.05(25) Å³, $V_0 = 423.48(24)$ Å³, and $V_0 = 461.57(23)$ Å³,
206 respectively. The fitting parameters under high-pressure and room-temperature yield $K_{T0} = 170$ (1)
207 GPa, $K_{T0}' = 3.74$ (22) for garnet, $K_{T0} = 121$ (2) GPa, $K_{T0}' = 3.90$ (35) for omphacite, and $K_{T0} = 122$
208 (1) GPa, $K_{T0}' = 2.51$ (16) for epidote, respectively.

209 To evaluate the quality of BM3-EoS fitting in this study, the relationship between the Eulerian
210 strain ($f_E = \left[(V_0/V)^{2/3} - 1 \right]$) and the normalized pressure ($F_E = P / \left[3f_E (2f_E + 1)^{5/2} \right]$) of
211 the main minerals for eclogite is plotted in Figure S3. Linear fitting of the three sets of data
212 exhibited a negative slope, indicating that the pressure derivative of the bulk modulus (K_{T0}') is less
213 than 4, which is consistent with our BM3-EoS fittings. The intercept value was obtained by
214 weighted linear regression of the data points, showing that $F_E(0) = 171$ (2) GPa for garnet,
215 $F_E(0) = 123$ (2) for omphacite, and $F_E(0) = 122$ (1) for epidote, respectively. The results are
216 consistent with the fitted isothermal bulk modulus ($K_{T0} = 170$ (1) GPa for garnet, $K_{T0} = 121$ (2)
217 GPa for omphacite, and $K_{T0} = 122$ (1) GPa for epidote, respectively) within the error range.

218 Accordingly, the K_{T0} and K_{T0}' obtained by the BM3-EoS fitting are reasonable. Using the V_0 fixed
219 at ambient conditions to fit third-order Birch-Murnaghan and Holland-Powell thermal-pressure
220 EoS (BM3-HP-EoS), the available EoS parameters, $K_{T0} = 170$ (1) GPa, $K_{T0}' = 3.82$ (14), and $\alpha_0 =$

221 $2.71 (5) \times 10^{-5} \text{ K}^{-1}$ for garnet; $K_{T0} = 121 (3) \text{ GPa}$, $K_{T0}' = 3.97 (34)$, and $\alpha_0 = 3.73 (20) \times 10^{-5} \text{ K}^{-1}$ for
222 omphacite; and $K_{T0} = 124 (2) \text{ GPa}$, $K_{T0}' = 2.04 (15)$, and $\alpha_0 = 3.04 (13) \times 10^{-5} \text{ K}^{-1}$ for epidote are
223 derived. The P - V - T data fitted through the BM3-HP-EoS model are shown in Figure 3.

224 **4.2 Comparison with previous studies**

225 **4.2.1 Garnet**

226 The thermal EoS parameters of garnet are obtained by fitting the P - V - T data to the BM3-EoS. We
227 compare our results with those of previous studies (Arimoto et al., 2015; Gréaux and Yamada,
228 2014; Lu et al., 2013; Milani et al., 2015, 2017; Xu et al., 2019; Zou et al., 2012). The K_{T0} of end-
229 member garnet, pyrope, almandine, grossular, and spessartine crystals is between 158 and 179
230 GPa, and the bulk modulus of almandine is the largest among the above (Table S3). From Table
231 S3, it can be seen that bulk modulus of powder XRD (Arimoto et al., 2015; Gréaux and Yamada,
232 2014; Pavese et al., 2001; Zou et al., 2012) are larger than those of single-crystal XRD (Milani et
233 al., 2015, 2017) with the same composition. The K_{T0} of solid solution garnets (Beyer et al., 2021;
234 Jiang et al., 2004; Lu et al., 2013; Xu et al., 2019) is also between 158 and 179 GPa mentioned
235 above and will be affected by the end-member components. The $K_{T0}=170 (1) \text{ GPa}$ in this study is
236 reasonable within this range. The obtained $K_{T0}'=3.82 (14)$ in this study is slightly lower than that
237 in previous studies. The Eulerian strain and the normalized pressure of the garnet shown in Figure
238 S3(a) exhibit a negative slope, which indicating K_{T0}' is less than 4. Moreover, compared with the
239 previous results, the obtained value of K_{T0}' in this study is within the error range (Supporting
240 Information Text S1). However, there is no obvious correlation between the fitted K_{T0} and K_{T0}' for
241 minerals of different compositions (Fig. S4); hence, the K_{T0} may not be precise when K_{T0}' is fixed.
242 For the α_0 , the andradite has the largest value ($3.16 (2) \times 10^{-5} \text{ K}^{-1}$), and the grossular has the

243 smallest value ($2.09 (2) \times 10^{-5} \text{ K}^{-1}$) among the end-member garnets. The thermal expansion
244 coefficient of $\text{Prp}_{21}\text{Alm}_{47}\text{Grs}_{31}\text{Sps}_1$ ($2.71 (5) \times 10^{-5} \text{ K}^{-1}$) in this study is comparable with previous
245 studies, but the influence of composition still needs to be considered.

246 **4.2.2 Omphacite**

247 Many studies have focused on the thermoelastic properties of omphacite (Hao et al., 2019;
248 Nishihara et al., 2003; Pandolfo et al., 2012b, 2012a; Xu et al., 2019; Zhang et al., 2016) (Table
249 S3). Most of the results are obtained by the single-crystal XRD method, except for the result of
250 Nishihara et al. (2003), which was obtained from powder XRD. K_{T0}' shows a higher value of 6.9
251 (12) in the study of Nishihara et al. (2003), while in others, K_{T0}' is between 4 and 5.7, and the
252 result of K_{T0}' (3.97) in this study is slightly lower than the above values. Additionally, according to
253 the results shown in Table S3, the bulk moduli of omphacite are in the range of 115-123 GPa. In
254 the study of Xu et al. (2019), an increase in the iron content would decrease K_{T0} , and they also
255 discussed the reasons for the discrepancy in K_{T0} in detail, such as the effective ionic radius,
256 pressure transmitting medium, and experimental pressure range. Comparing our results with Xu et
257 al. (2019), we conclude that the incorporation of Fe would reduce the bulk modulus. However,
258 except for Fe content, there does not seem to be a significant correlation between the other
259 components and the bulk modulus of omphacite. The α_0 of the Di-Jd solid solution is similar (2.64
260 $(2) \times 10^{-5} \text{ K}^{-1}$ - $2.8 (3) \times 10^{-5} \text{ K}^{-1}$) but less than that of $\text{Quad}_{48}\text{Jd}_{45}\text{Ae}_7$ ($3.73 (20) \times 10^{-5} \text{ K}^{-1}$) and
261 $\text{Quad}_{53}\text{Jd}_{27}\text{Ae}_{20}$ ($3.4 (4) \times 10^{-5} \text{ K}^{-1}$). It may be inferred that the Ae contents affect thermal expansion.

262 **4.2.3 Epidote**

263 The thermal EoS parameters of epidote in this study are compared with those reported in previous
264 studies (Fan et al., 2014; Gatta et al., 2011; Holland et al., 1996; Li et al., 2020; Qin et al., 2016)

265 (Table S3). Although the bulk modulus appears to be related to the Fe^{3+} content, it does not show a
266 good correlation. Increasing the content of Fe^{3+} can enhance the bulk modulus, but the result in
267 Holland et al. (1996) shows an abnormally large value of 162 (4) GPa, which is much higher than
268 the 111-133 GPa resulting from other studies. This may be attributed to the fixed K_{T0}' at 4 and
269 powder XRD methods used in the study of Holland et al. (1996). Furthermore, the K_{T0}' obtained
270 from powder XRD (Fan et al., 2014; Gatta et al., 2011) is also larger than that from single-crystal
271 XRD (Qin et al., 2016). The possible reasons for these discrepancies are complicated. Li et al.
272 (2020) conducted a detailed study on this topic. Previous studies on α_0 and $(\partial K_T / \partial T)_P$ of epidote
273 are limited. The α_0 ($3.04 (13) \times 10^{-5} \text{ K}^{-1}$) in this study is lower than that of Gatta et al. (2011) (5.1
274 ($2) \times 10^{-5} \text{ K}^{-1}$) and Li et al. (2020) ($3.8 (5) \times 10^{-5} \text{ K}^{-1}$).

275

276 **5 Implications**

277 In the Himalayan-Tibetan system, lithospheric removal is proposed to occur in either the breakoff
278 of the subducted slab of the Indian continental lithosphere (Chung et al., 2005; Turner et al., 1993)
279 or convective removal of the thickened lower part of the lithosphere (Miller et al., 1999). The
280 metamorphic eclogitization taking place in the subducted slab and the lowermost crust has been
281 deduced as the possible cause of subducted slab break-off and the convective removal of the lower
282 crust (Krystopowicz and Currie, 2013). Increased density in the eclogitized subducted slab and the
283 lower crust will promote the above two lithospheric removal modes if the lower crust is weak
284 enough for the negative buoyancy of the mantle lithosphere to be detached. Therefore, to better
285 consider the role of eclogite density variations in the process of lithospheric removal, we model
286 the density of minerals and eclogite aggregates along with the geotherms of Tibet and discuss the

287 effects of the degree of eclogitization on lithospheric removal.

288 The eclogite chemical data collected in Tibet and examined in our study come from a great
289 number of eclogite samples collected in previous studies (e.g. Chan et al., 2009; Liu et al., 2019;
290 Yang et al., 2009; Zhai et al., 2011a). The eclogite samples consist of garnet, omphacite, epidote,
291 amphibole, zoisite, symplectite along with minor phengite, quartz, rutile, and rare apatite, ilmenite,
292 and titanite as accessory minerals. Since the eclogite samples have suffered retrograde
293 metamorphism, we assume that is largely composed of garnet and omphacite plus slight epidote
294 before retrograde metamorphism. The accessory phases observed in natural eclogite are excluded
295 because of their minimal abundance of less than 5%. Based on the mineral composition data of
296 exposed eclogite in Tibet (Fig. S6) (e.g. Cheng et al., 2015; Dong et al., 2018; Huang et al., 2015;
297 Jin et al., 2019; Li et al., 2017; Zhai et al., 2011b, 2011a), the components of eclogite are 50
298 vol. % garnet + 45 vol. % omphacite + 5 vol. % epidote (parameterized as a value out of 100)
299 using the normal distribution.

300 We take into account two different delamination modes, namely, delamination caused by the
301 separation of the Neo-Tethyan slab (detachment of the subducted Neo-Tethyan oceanic slab) in the
302 Paleozoic and convective removal of the lower crust of the subducted Indian continent beneath the
303 Lhasa terrane during the Cenozoic. The temperature and pressure conditions of exposed eclogites
304 in the Paleozoic and Cenozoic are somewhat consistent with the geothermal lines provided by
305 previous studies (Fig. S7). The two different delamination modes reflect relatively cold geotherms
306 and hot geotherms, respectively. Therefore, these geothermal lines are used in our models. The
307 thermal EoS parameters of eclogitic garnet, omphacite, and epidote are derived through the **BM3-**
308 **HP-EoS** shown in supporting information Table S2.

309 **5.1 The density of main minerals for eclogite along the geothermal profile in Tibet**

310 Tibetan eclogite is mainly composed of garnet, and omphacite, with a few epidotes. As shown in
311 Figure 2, the exposed minerals differ in composition. The specific composition of minerals
312 constrains the density. Therefore, we refer to the thermoelastic parameters of Xu et al. (2019) and
313 Nishihara et al. (2003) to depict the density distribution of different components (Fe content) of
314 garnet and omphacite under Tibetan geothermal lines, respectively. The corresponding
315 thermoelastic parameters can be seen in Table S3. The mineral compositions of previous studies
316 are within the range of the Tibetan constituents collected in this study (Fig. 2).

317 The density distribution of minerals along with relatively cold Tibetan geothermal conditions is
318 shown in Figure 4 (the results along with hot geotherms can be seen in supporting information Fig.
319 S8). The result clearly shows that the density of garnet is linked with the iron content. The density
320 of garnet ($\text{Prp}_{21}\text{Alm}_{47}\text{Grs}_{31}\text{Sps}_1$, with 47 mol. % almandine) in this study is higher than that of
321 low-Fe garnet ($\text{Prp}_{28}\text{Alm}_{38}\text{Grs}_{33}\text{Sps}_1$, with 38 mol. % almandine) (Xu et al., 2019) by **2.22%** but
322 lower than that of high-Fe garnet ($\text{Prp}_{14}\text{Alm}_{62}\text{Grs}_{19}\text{Adr}_3\text{Sps}_2$, with 62 mol. % almandine) (Xu et al.,
323 2019) by **3.82%** at ~80 km (Fig. 4a). With increasing depth, the density of high-Fe garnet
324 increases by a larger amplitude. This discrepancy may be caused by its smaller degree of thermal
325 expansion ($2.56 (44) \times 10^{-5} \text{ K}^{-1}$). Accordingly, the influence of pressure on the density is greater
326 than that of temperature, which leads to faster increases in density with depth. The density of
327 omphacite does not show obvious characteristics related to its composition. The density of
328 omphacite ($\text{Quad}_{48}\text{Jd}_{45}\text{Ae}_7$, with 7 mol. % aegirine) in this study is lower than that of high-Fe
329 omphacite ($\text{Quad}_{53}\text{Jd}_{27}\text{Ae}_{20}$, with 20 mol. % aegirine) (Xu et al., 2019), $\text{Quad}_{72}\text{Jd}_{28}$ (Nishihara et
330 al., 2003), and $\text{Quad}_{57}\text{Jd}_{42}\text{Ae}_1$ (with 1 mol. % aegirine) (Xu et al., 2019) by 1.95%, 1.47%, and

331 0.83%, respectively, at ~80 km (Fig. 4b). The presence of iron in certain quantities does increase
332 the density of omphacite, but the density of omphacite is also affected by other elements, such as
333 calcium and magnesium. Moreover, thermal EoS parameters are also of vital importance to
334 calculate the density. The relatively low thermal expansion of $\text{Quad}_{72}\text{Jd}_{28}$ ($2.7 (3) \times 10^{-5} \text{ K}^{-1}$) and
335 $\text{Quad}_{57}\text{Jd}_{42}\text{Ae}_1$ (with 1 mol. % aegirine) ($2.8 (3) \times 10^{-5} \text{ K}^{-1}$) may further enhance the increasing rate
336 of density with depth. It is worth noting that the densities of $\text{Quad}_{48}\text{Jd}_{45}\text{Ae}_7$ (with 7 mol. %
337 aegirine) in this study and $\text{Quad}_{57}\text{Jd}_{42}\text{Ae}_1$ (with 1 mol. % aegirine) of Xu et al. (2019) are the same
338 under ambient conditions but inconsistent under high-pressure and high-temperature conditions.
339 Therefore, the K_{T0} and K_{T0}' of the two omphacites are somewhat consistent with each other, while
340 the thermal expansion and $(\partial K_T / \partial T)_P$ are different. Collectively, the thermal EoS parameters are of
341 the essence in the derivation of the mineral density.

342 **5.2 The density of eclogite in Tibet**

343 Eclogitized crust and lithospheric mantle may be potential factors causing delamination (Faccenda
344 et al., 2009; Krystopowicz and Currie, 2013). The density of eclogite and peridotite can provide
345 new constraints to control the breakoff of the subducted slab and convective removal of the
346 lithosphere in the process of delamination. Therefore, we plot the density distribution of eclogite
347 with different garnet contents and peridotite along the Paleozoic and Cenozoic Tibetan geotherms,
348 as shown in Figure 5. In our model, the mineral composition of Tibetan eclogite is in the range of
349 40 vol. % garnet + 55 vol. % omphacite + 5 vol. % epidote to 60 vol. % garnet + 35 vol. %
350 omphacite + 5 vol. % epidote based on the exposed eclogite in Tibet (the composition of epidote is
351 only 5 vol. % default due to its low content in this study). The composition of surrounding
352 peridotite consists of 70 vol. % olivine + 25 vol. % orthopyroxene + 3 vol. % clinopyroxene + 2

353 vol. % spinel (Yang et al., 2019; Zhao et al., 2021). The densities of eclogite and peridotite
354 aggregates are obtained considering their arithmetic mean. The densities of each mineral under
355 specific temperature and pressure conditions are derived by the following formula:

$$356 \quad \rho(T, P) = \frac{V(T, 0)}{V(T, P)} \times \frac{Z \times M}{N_a \times V_0} \quad (4)$$

357 where V_0 is the reference unit cell volume at ambient conditions, M is molecular weight, Z is the
358 number of formula units in the unit cell and N_a is the Avogadro number.

359 Most changes in the deep conditions of the Earth are progressing slowly, so there is adequate
360 time for recrystallization to relieve the maximum stress point (Robertson, 1988; Skinner, 1966).

361 Here, we assume that the elastic-plastic interaction among different minerals and possible
362 deviations from hydrostatic conditions are ignored and the density of the eclogite aggregate can be
363 obtained by the arithmetic mean as follows:

$$364 \quad \bar{\rho} = \sum \lambda_i \rho_i(T, P) \quad (5)$$

365 where the subscript i denotes the i th mineral of the upper mantle, and λ is the volume proportion
366 of each mineral.

367 The densities of Tibetan eclogite (with the garnet composition of $\text{Prp}_{21}\text{Alm}_{47}\text{Grs}_{31}\text{Sps}_1$, the
368 omphacite composition of $\text{Quad}_{48}\text{Jd}_{45}\text{Ae}_7$, and the epidote composition of
369 $\text{Ca}_{2.02}\text{Fe}_{0.75}\text{Al}_{2.32}\text{Si}_{0.16}(\text{SiO}_4)(\text{Si}_2\text{O}_7\text{O(OH)})$) and peridotite (with the olivine composition of
370 $\text{Fo}_{89.9}\text{Fa}_{10.1}$, the orthopyroxene composition of $\text{En}_{89.6}\text{Fs}_{9.7}\text{Wo}_{0.7}$, the clinopyroxene composition of
371 $\text{Quad}_{88.5}\text{Jd}_{11.5}$, and the spinel composition of $(\text{Mg}_{0.790}\text{Fe}_{0.204}\text{Ni}_{0.005}\text{Ti}_{0.001})_{1.000}(\text{Al}_{0.821}\text{Cr}_{0.158}\text{Fe}_{0.021})_{2.002}\text{O}_4$) in this study along the Paleozoic
372 geothermal line are shown in Figure 5a. The results show that the increase in garnet has a
373 profound influence on the density of eclogite. For every 10% increase in garnet, the density of
374

375 eclogite increases by ~1.7%. The garnet content in Tibetan eclogite is estimated to be 40 vol. %-60
376 vol. % (Fig. S6). The densities of this part of eclogite are **3.54-3.66 g/cm³**, which is approximately
377 **7.4%-11.2%** more than that of peridotite (3.29 g/cm³) at ~80 km. The density difference between
378 eclogite and peridotite is 0.24 g/cm³-0.37 g/cm³ (Fig. 5b). At the same time, we also consider the
379 density of eclogite aggregates without epidote (Fig. S6). The results show that 5 vol. % epidote
380 has little effect on the density of eclogite, especially eclogite with garnet contents of 50 vol. %-60
381 vol. % (Fig. S9). To account for the role of iron, the density distributions of high-Fe
382 (Prp₁₄Alm₆₂Grs₁₉Adr₃Sps₂ and Quad₅₃Jd₂₇Ae₂₀ and low-Fe eclogite (Prp₂₈Alm₃₈Grs₃₃Sps₁ and
383 Quad₅₇Jd₄₂Ae₁) are plotted to better constrain the range of eclogite density (Fig. S10) (Xu et al.,
384 2019). For high-Fe and low-Fe eclogites, the densities of eclogite increase by ~1.9% and ~1.4%
385 for each 10% increase in garnet, respectively. The densities of eclogite are 3.64 g/cm³-3.78 g/cm³
386 for high-Fe content and 3.53 g/cm³-3.63 g/cm³ for low-Fe content at ~80 km. Furthermore, the
387 densities of high-Fe and low-Fe eclogites are 10.6%-14.9% and 7.2%-10.3% higher than the
388 surrounding peridotite, respectively. For a more straightforward comparison, taking eclogite
389 containing 50 vol. % garnet as an example (Fig. S11), the densities of high-Fe eclogite, low-Fe
390 eclogite, and Tibetan eclogite at ~80 km are 3.71 g/cm³, 3.58 g/cm³, and 3.61 g/cm³, respectively.
391 An increase in the iron content can substantially increase the density of eclogite, although it will
392 be constrained by the thermal EoS parameters of minerals.

393 Similarly, we also discuss the density profile along the Cenozoic geothermal line, which can be
394 seen in supporting information Text S2. In any case, the density difference caused by eclogite may
395 be one of the prominent factors instigating the delamination process.

396 **5.3 Influence of the degree of eclogitization on the density of the subducted slab**

397 Eclogite in the mantle, which is believed to be 5%-10% denser than peridotite (Garber et al.,
398 2018), is responsible for the excess compositional density. Furthermore, some calculations
399 propose that the degree of eclogitization of the subducted slab is a key factor in the delamination
400 process (Matchette-Downes et al., 2019). To investigate the influence of the degree of
401 eclogitization in the delamination process, we plot the density variations with different mineral
402 compositions under different degrees of eclogitization (Fig. 6). **We consider eclogitization in the**
403 **lithospheric mantle of the subducted slab, here the degree of eclogitization refers to the amount of**
404 **eclogite in the lithospheric mantle. In our preferred model, the 7-km thick subducted oceanic crust**
405 **becomes eclogite, while the lithospheric mantle constrains a different amount of eclogite.** Since
406 the subducted Indian oceanic slab might be fragmented into several pieces, the longitudinal size of
407 the fractured slab is postulated to be 60 km (Peng et al., 2016). Our estimated average density of
408 the fragmented slab with various degrees of eclogitization is shown in Figure 6a. The results
409 clearly show that the density increases monotonically with the garnet content and the degree of
410 eclogitization. The garnet content is of profound importance to the density of eclogite. The higher
411 the proportion of garnet is, the greater the density increases with increasing degrees of
412 eclogitization. The garnet content in Tibetan eclogite is estimated to be between 40-60 vol. %.
413 Taking garnet with an average volume percentage of 50 vol. % in Tibetan eclogite as an example,
414 the density of eclogitized subducted slabs ranges from **3.35** g/cm³ with 10% eclogitization to **3.61**
415 g/cm³ with 100 vol. % eclogitization. For a garnet content of 50 vol.%, the density increases by
416 **0.029** g/cm³ per 10 vol. % increase in the degree of eclogitization. The density will increase with
417 increasing garnet contents, from **0.006** g/cm³ for 10 vol. % to **0.051** g/cm³ for 90 vol. %. The
418 densities of high-Fe and low-Fe eclogitized fragmented slabs are also shown in Figure S12. The

419 high-Fe content shows that the density variation increases with the degree of eclogitization from
420 0.007 g/cm³ for 10 vol. % to 0.064 g/cm³ for 90 vol. % garnet, while the low-Fe content shows a
421 density change from 0.004 g/cm³ for 10 vol. % garnet to 0.045 g/cm³ for 90 vol. % garnet.

422 **5.4 Delamination in Tibet**

423 The development of delamination is associated with the instability of the lower crust and the
424 mantle lithosphere. The eclogitization of the subducted slab and lower crust plays a vital role in
425 the process of delamination due to the high density of eclogite, which makes the formation denser
426 than the surrounding mantle lithosphere and provides critical negative buoyancy (Gögüş and Ueda,
427 2018; Krystopowicz and Currie, 2013). The densities of the eclogitic lower crust and mantle
428 lithosphere during slab subduction and convective removal are sufficiently higher than that of the
429 asthenosphere and are good candidates for the initiation of destabilization.

430 **5.4.1 Subducted slab breakoff**

431 A series of collisional breakoff events is proposed to have occurred throughout 60-45 Ma in Tibet
432 (Chung et al., 2005, 2009; Ma et al., 2014; Zhu et al., 2015). The formation of eclogite
433 presumably kick-starts slab breakoff during the subduction of the Indian oceanic plate underthrust
434 below the southern margin of Tibet. The subducted Indian oceanic slab fragmented into several
435 pieces, due to what has been identified as a high-velocity anomaly (Peng et al., 2016; Shi et al.,
436 2020b). The seismological evidence of high density (Hetényi et al., 2007), high V_P (Schulte-
437 Pelkum et al., 2005), and low longitudinal/transverse (V_P/V_S) ratios (Wittlinger et al., 2009) further
438 confirms that there may be variable degrees of eclogitization beneath Tibet. Figure 6 shows the
439 density profile of subducted slabs with different garnet compositions, different degrees of
440 eclogitization, and variable densities compared with the surrounding peridotite. An increasing

441 degree of eclogitization and an enhanced garnet content in eclogite increases the density difference
442 between the slab and the surrounding peridotite. Previous studies have made preliminary estimates
443 of the average density from the isostatic balance and geoid anomalies and postulated that the
444 density excess could be between 0-0.19 g/cm³ (Matchette-Downes et al., 2019). For Tibetan
445 eclogite containing 40 vol. %-60 vol. % garnet, if the lithospheric mantle is a mixture of peridotite
446 and eclogite with a density anomaly of 0.19 g/cm³, our model requires a range of **44%-70%**
447 degrees of eclogitization. If the eclogite is high-Fe, only a 30%-48% degree of eclogitization is
448 needed to produce the density difference (Fig. S12), while an eclogitization degree is in the range
449 of 49%-74% is needed for the low-Fe eclogite. However, some seismological data show that the
450 crust or lithospheric mantle being only ~30% eclogitized might cause gravitational instability in
451 Tibet (Matchette-Downes et al., 2019; Shi et al., 2020a), which is lower than our estimation. Our
452 results clearly show that density excess is closely linked with garnet content and eclogitization
453 degree. If eclogite has a high garnet content, a relatively low degree of eclogitization could
454 instigate the delamination of slab breakoff.

455 On the other hand, the presence of a weak lower crust and a vertical conduit to accommodate
456 asthenosphere influx is also necessary for the delamination process. The weak layer between the
457 residual crustal and downward peeling lithosphere layer (and/or lower crust) (Gögüs and Ueda,
458 2018) could promote the initiation and propagation of delamination. Therefore, very high
459 temperatures and relatively low lower-crustal viscosities are also other controlling factors of
460 delamination (Gögüs and Pysklywec, 2008; Morency, 2004). Here, we assume that the length of
461 the fractured slab is 60 km, which drops 80 km over 45 Ma and that the viscosity of the
462 asthenosphere is $5*10^{20}$ Pa·S (Wang et al., 2019). By using Stokes' Law (Supporting Information

463 Text S3), ignoring the thermal disturbance, and assuming the most ideal conditions, the density
464 difference caused by eclogite needs to be at least 0.15 g/cm³ to produce such delamination. The
465 result is close to those discussed above in gravity anomalies.

466 In particular, the presence of eclogite with a greater abundance of garnet, a higher-Fe content,
467 and a greater degree of eclogitization would instigate the delamination process of slab breakoff.

468 **5.4.2 Removal of the eclogitized lower crust**

469 The thickened lower crust undergoes “convective removal” due to gravitational instability, which
470 is another type of delamination that occurred in Tibet from 25 Ma to 0 Ma (Chung et al., 2005;
471 Nomade et al., 2004). The convective removal of the lithosphere during delamination corresponds
472 to higher temperature conditions (Craig et al., 2020). In this circumstance, the density of Tibetan
473 eclogite is 6.9%-10.8% denser than the surrounding peridotite at ~60 km (Fig. 5b), which is
474 analogous to the results in the case of subducted slab detachment. This result is also in ample
475 agreement with the result obtained by Garber et al. (2018), which noted that eclogite is 5%-10%
476 denser than peridotite. The density difference between eclogite and peridotite is 0.22 g/cm³-0.35
477 g/cm³ with 40 vol. %-60 vol. % garnet in Tibet (Fig. 5d). During this stage, it is believed that
478 delamination of the thickened, eclogitized lower crust has occurred. Similarly, Stokes’ law can be
479 used considering ideal conditions without any thermal disturbance. If the falling block is assumed
480 to be approximately 30 km in the longitudinal direction and the viscosity of the asthenosphere is
481 5*10²⁰ Pa·S, the falling block can drop by 70-110 km within 25 Ma. For eclogite with a high-Fe
482 content, a density difference of 0.35 g/cm³-0.50 g/cm³ makes the fragmented block capable of
483 falling 105-155 km, while the density difference of 0.24 g/cm³-0.33 g/cm³ with a low-Fe content
484 makes the block able to fall 75-102 km (Fig. S13). The fragmented block with a high-Fe content

485 can fall a larger distance at the same time, indicating that the high-Fe content is more likely to
486 promote the occurrence of delamination. This result is consistent with the high-velocity
487 anomalous blocks identified at 100-200 km by seismic tomography (Peng et al., 2016; Shi et al.,
488 2016, 2020a).

489 In summary, density contrasts can provide a stimulus for the initiation of instability. It is accepted
490 that eclogite with a high garnet content and a high Fe content and a high proportion of eclogite in
491 the lithospheric mantle may have strongly promoted delamination during the process of India-Asia
492 collision from the perspective of density.

493

494 **6. Conclusion**

495 The P - V - T EoS of the main minerals of eclogite is combined with its mineral composition
496 and the geothermal line to derive the density of Tibetan eclogite in this study. We offer a new
497 perspective by obtaining the thermal EoS for the main minerals of eclogite in a single experiment.
498 The thermal EoS parameters of the main minerals of eclogite are derived by fitting the P - V - T data
499 to the HT-BM-EoS. The density of minerals along the Tibetan geotherm shows that the density is
500 closely related to its composition and thermal EoS parameters. Increasing iron contents increase
501 the density of minerals, but if the molecular masses of two minerals are similar, the thermal EoS
502 parameters play a pivotal role. The garnet content profoundly increases the density of eclogite. For
503 every 10 vol. % increase in garnet, the density of eclogite increases by approximately 1.7%. The
504 density of Tibetan eclogite is approximately 7-11% denser than that of the surrounding peridotite.
505 An increasing proportion of garnet, Fe content, and degree of eclogitization enhance the density
506 difference to facilitate the delamination process. For Tibetan eclogite containing 40-60 vol. %

507 garnet, 44-70% degrees of eclogitization can produce the same density difference as obtained by
508 the isostatic balance and the geoid anomaly. According to a rough calculation, the fragmented
509 block will fall 70-155 km. A high-Fe content is more likely to promote delamination. Eclogite is a
510 good candidate for the initiation of instability and may be more susceptible to inducing the
511 breakoff of the subducted slab or the gravitational removal of the lower crust during the process of
512 the India-Asia collision.

513

514 **Data availability**

515 All the data presented in this paper are available upon request.

516

517 **Author contributions**

518 All authors contributed to the preparation and revision of the manuscript. Z. Ye: Data curation,
519 Investigation, Formal analysis, Writing-original draft, Writing-review & editing. D. Fan:
520 Investigation, Conceptualization, Supervision, Methodology, Funding acquisition, Writing-review
521 & editing. B. Li: Data curation, Writing-review & editing. Q. Tang: Software, Validation, Writing-
522 review & editing. J. Xu: Investigation, Supervision, Writing-review & editing. D. Zhang: Formal
523 analysis, Writing-review & editing. W. Zhou: Investigation, Conceptualization, Supervision,
524 Writing-review & editing.

525

526 **Competing interests**

527 The authors declare that they have no conflict of interest.

528

529 **Disclaimer**

530 Publisher's note: Copernicus Publications remains neutral regard to jurisdictional claims in
531 published maps and institutional affiliations.

532

533 **Acknowledgments**

534 This project was funded by the National Natural Science Foundation of China (Grant Nos.
535 42172048, U2032118 and 41802043), the Youth Innovation Promotion Association CAS (Dawei
536 Fan, 2018434), the Chinese Academy of Sciences "Light of West China" Program (2019), the
537 Guizhou Provincial Science and Technology Projects (QKHJC-ZK[2021]ZD042), and the
538 Innovation and Entrepreneurship Funding of High-Level Overseas Talents of Guizhou Province
539 (Dawei Fan, [2019] 10).

540

541 **Supplementary Information.** The supplementary information describes the density profile of
542 garnet at high temperature, density profile along Cenozoic geothermal line, data of unit-cell
543 parameters of eclogite minerals, thermal EoS parameters of this study and previous researches,
544 figures of Eulerian finite strain-normalized pressure (F_E - f_E), isothermal bulk modulus (K_{T0}) and its
545 pressure derivative (K_{T0}') plot of garnet and omphacite, normal distribution of eclogite minerals,
546 density evolution of minerals, and density profile of different Fe-content eclogite.

547

548 **References:**

549 Angel, R. J., Alvaro, M. and Gonzalez-Platas, J.: EosFit7c and a Fortran module (library) for equation
550 of state calculations, Zeitschrift für Krist. - Cryst. Mater., 229(5), doi:10.1515/zkri-2013-1711, 2014.
551 Angel, R. J., Alvaro, M. and Nestola, F.: 40 years of mineral elasticity: a critical review and a new

552 parameterisation of equations of state for mantle olivines and diamond inclusions, *Phys. Chem. Miner.*,
553 45(2), 95–113, doi:10.1007/s00269-017-0900-7, 2018.

554 Arimoto, T., Gréaux, S., Irifune, T., Zhou, C. and Higo, Y.: Sound velocities of $\text{Fe}_3\text{Al}_2\text{Si}_3\text{O}_{12}$
555 almandine up to 19 GPa and 1700 K, *Phys. Earth Planet. Inter.*, 246, 1–8,
556 doi:10.1016/j.pepi.2015.06.004, 2015.

557 Beyer, C., Kurnosov, A. V., Ballaran, T. B. and Frost, D. J.: High-pressure and high-temperature
558 single-crystal X-ray diffraction of complex garnet solid solutions up to 16 GPa and 823 K, *Phys. Chem.*
559 *Miner.*, 48(4), 17, doi:10.1007/s00269-021-01139-5, 2021.

560 Birch, F.: Finite Elastic Strain of Cubic Crystals, *Phys. Rev.*, 71(11), 809–824,
561 doi:10.1103/PhysRev.71.809, 1947.

562 Birch, F.: Finite strain isotherm and velocities for single-crystal and polycrystalline NaCl at high
563 pressures and 300 K, *J. Geophys. Res.*, 83(B3), 1257, doi:10.1029/JB083iB03p01257, 1978.

564 Bird, P.: Initiation of intracontinental subduction in the Himalaya, *J. Geophys. Res. Solid Earth*,
565 83(B10), 4975–4987, doi:10.1029/JB083iB10p04975, 1978.

566 Bird, P.: Continental delamination and the Colorado Plateau, *J. Geophys. Res. Solid Earth*, 84(B13),
567 7561–7571, doi:10.1029/JB084iB13p07561, 1979.

568 Chan, G. H. N., Waters, D. J., Searle, M. P., Aitchison, J. C., Horstwood, M. S. A., Crowley, Q., Lo, C.
569 H. and Chan, J. S. L.: Probing the basement of southern Tibet: evidence from crustal xenoliths
570 entrained in a Miocene ultrapotassic dyke, *J. Geol. Soc. London.*, 166(1), 45–52, doi:10.1144/0016-
571 76492007-145, 2009.

572 Chen, W. and Tenzer, R.: The application of a gravimetric forward modelling of the lithospheric
573 structure for an estimate of the average density of the upper asthenosphere, *Geod. Geodyn.*, 10(4), 265–

574 275, doi:10.1016/j.geog.2019.04.003, 2019.

575 Cheng, H., Zhang, C., Vervoort, J. D., Lu, H., Wang, C. and Cao, D.: Zircon U–Pb and garnet Lu–Hf
576 geochronology of eclogites from the Lhasa Block, Tibet, *Lithos*, 155, 341–359,
577 doi:10.1016/j.lithos.2012.09.011, 2012.

578 Cheng, H., Liu, Y., Vervoort, J. D. and Lu, H.: Combined U–Pb, Lu–Hf, Sm–Nd and Ar–Ar
579 multichronometric dating on the Bailang eclogite constrains the closure timing of the Paleo-Tethys
580 Ocean in the Lhasa terrane, Tibet, *Gondwana Res.*, 28(4), 1482–1499, doi:10.1016/j.gr.2014.09.017,
581 2015.

582 Chung, S.-L., Chu, M.-F., Zhang, Y., Xie, Y., Lo, C.-H., Lee, T.-Y., Lan, C.-Y., Li, X., Zhang, Q. and
583 Wang, Y.: Tibetan tectonic evolution inferred from spatial and temporal variations in post-collisional
584 magmatism, *Earth-Science Rev.*, 68(3–4), 173–196, doi:10.1016/j.earscirev.2004.05.001, 2005.

585 Chung, S.-L., Chu, M.-F., Ji, J., O'Reilly, S. Y., Pearson, N. J., Liu, D., Lee, T.-Y. and Lo, C.-H.: The
586 nature and timing of crustal thickening in Southern Tibet: Geochemical and zircon Hf isotopic
587 constraints from postcollisional adakites, *Tectonophysics*, 477(1–2), 36–48,
588 doi:10.1016/j.tecto.2009.08.008, 2009.

589 Conrad, C. P. and Molnar, P.: Convective instability of a boundary layer with temperature-and strain-
590 rate-dependent viscosity in terms of “available buoyancy,” *Geophys. J. Int.*, 139(1), 51–68,
591 doi:10.1046/j.1365-246X.1999.00896.x, 1999.

592 Corrie, S. L., Kohn, M. J. and Vervoort, J. D.: Young eclogite from the Greater Himalayan Sequence,
593 Arun Valley, eastern Nepal: P–T–t path and tectonic implications, *Earth Planet. Sci. Lett.*, 289(3–4),
594 406–416, doi:10.1016/j.epsl.2009.11.029, 2010.

595 Craig, T. J., Kelemen, P. B., Hacker, B. R. and Copley, A.: Reconciling Geophysical and Petrological

596 Estimates of the Thermal Structure of Southern Tibet, *Geochemistry, Geophys. Geosystems*, 21(8),

597 doi:10.1029/2019GC008837, 2020.

598 DeCelles, P. G., Robinson, D. M. and Zandt, G.: Implications of shortening in the Himalayan fold-

599 thrust belt for uplift of the Tibetan Plateau, *Tectonics*, 21(6), 12-1-12-25, doi:10.1029/2001TC001322,

600 2002.

601 Dera, P., Zhuravlev, K., Prakapenka, V., Rivers, M. L., Finkelstein, G. J., Grubor-Urosevic, O.,

602 Tschauner, O., Clark, S. M. and Downs, R. T.: High pressure single-crystal micro X-ray diffraction

603 analysis with GSE ADA/RSV software, *High Press. Res.*, 33(3), 466–484,

604 doi:10.1080/08957959.2013.806504, 2013.

605 Dong, Y.-L., Wang, B.-D., Zhao, W.-X., Yang, T.-N. and Xu, J.-F.: Discovery of eclogite in the

606 Bangong Co–Nujiang ophiolitic mélange, central Tibet, and tectonic implications, *Gondwana Res.*, 35,

607 115–123, doi:10.1016/j.gr.2016.03.010, 2016.

608 Dong, Y., Xie, C., Yu, Y., Wang, B., Li, L. and Zeng, X.: The discovery of Longyasongduo eclogite

609 from Gongbujiangda County, Tibet, and its significance., *Geol. Bull. Of China*, 37(8), 2018.

610 Ehlers, T. A. and Poulsen, C. J.: Influence of Andean uplift on climate and paleoaltimetry estimates,

611 *Earth Planet. Sci. Lett.*, 281(3–4), 238–248, doi:10.1016/j.epsl.2009.02.026, 2009.

612 Faccenda, M., Minelli, G. and Gerya, T. V.: Coupled and decoupled regimes of continental collision:

613 Numerical modeling, *Earth Planet. Sci. Lett.*, 278(3–4), 337–349, doi:10.1016/j.epsl.2008.12.021, 2009.

614 Faccincani, L., Faccini, B., Casetta, F., Mazzucchelli, M., Nestola, F. and Coltorti, M.: EoS of mantle

615 minerals coupled with composition and thermal state of the lithosphere: Inferring the density structure

616 of peridotitic systems, *Lithos*, 404–405(September), 106483, doi:10.1016/j.lithos.2021.106483, 2021.

617 Fan, D., Xu, J., Wei, S., Chen, Z. and Xie, H.: In-situ high-pressure synchrotron X-ray diffraction of

618 natural epidote, Chin. J. High Press. Phys., 28, 257–261, doi:10.11858/gjwlxb.2014.03.001, 2014.

619 Fei, Y., Ricolleau, A., Frank, M., Mibe, K., Shen, G. and Prakapenka, V.: Toward an internally

620 consistent pressure scale, Proc. Natl. Acad. Sci., 104(22), 9182–9186, doi:10.1073/pnas.0609013104,

621 2007.

622 Finkelstein, G. J., Jackson, J. M., Sturhahn, W., Zhang, D., Alp, E. E. and Toellner, T. S.: Single-

623 crystal equations of state of magnesiowüstite at high pressures, Am. Mineral., 102(8), 1709–1717,

624 doi:10.2138/am-2017-5966, 2017.

625 Garber, J. M., Maurya, S., Hernandez, J., Duncan, M. S., Zeng, L., Zhang, H. L., Faul, U., McCammon,

626 C., Montagner, J., Moresi, L., Romanowicz, B. A., Rudnick, R. L. and Stixrude, L.: Multidisciplinary

627 Constraints on the Abundance of Diamond and Eclogite in the Cratonic Lithosphere, Geochemistry,

628 Geophys. Geosystems, 19(7), 2062–2086, doi:10.1029/2018GC007534, 2018.

629 Gatta, G. D., Merlini, M., Lee, Y. and Poli, S.: Behavior of epidote at high pressure and high

630 temperature: a powder diffraction study up to 10 GPa and 1200 K, Phys. Chem. Miner., 38(6), 419–428,

631 doi:10.1007/s00269-010-0415-y, 2011.

632 Göğüş, O. H. and Pysklywec, R. N.: Near-surface diagnostics of dripping or delaminating lithosphere, J.

633 Geophys. Res., 113(B11), B11404, doi:10.1029/2007JB005123, 2008.

634 Göğüş, O. H. and Ueda, K.: Peeling back the lithosphere: Controlling parameters, surface expressions

635 and the future directions in delamination modeling, J. Geodyn., 117(March), 21–40,

636 doi:10.1016/j.jog.2018.03.003, 2018.

637 Gottschalk, M.: Thermodynamic Properties of Zoisite, Clinozoisite and Epidote, Rev. Mineral.

638 Geochemistry, 56(1), 83–124, doi:10.2138/gsrmg.56.1.83, 2004.

639 Gréaux, S. and Yamada, A.: P-V-T equation of state of $Mn_3Al_2Si_3O_{12}$ spessartine garnet, Phys. Chem.

640 Miner., 41(2), 141–149, doi:10.1007/s00269-013-0632-2, 2014.

641 Guillot, S., Mahéo, G., de Sigoyer, J., Hattori, K. H. and Pêcher, A.: Tethyan and Indian subduction

642 viewed from the Himalayan high- to ultrahigh-pressure metamorphic rocks, Tectonophysics, 451(1–4),

643 225–241, doi:10.1016/j.tecto.2007.11.059, 2008.

644 Hacker, B. R.: Hot and Dry Deep Crustal Xenoliths from Tibet, Science (80), 287(5462), 2463–2466,

645 doi:10.1126/science.287.5462.2463, 2000.

646 Hao, M., Zhang, J. S., Pierotti, C. E., Ren, Z. and Zhang, D.: High-Pressure Single-Crystal Elasticity

647 and Thermal Equation of State of Omphacite and Their Implications for the Seismic Properties of

648 Eclogite in the Earth's Interior, J. Geophys. Res. Solid Earth, 124(3), 2368–2377,

649 doi:10.1029/2018JB016964, 2019.

650 He, Y., Li, S., Hoefs, J., Huang, F., Liu, S.-A. and Hou, Z.: Post-collisional granitoids from the Dabie

651 orogen: New evidence for partial melting of a thickened continental crust, Geochim. Cosmochim. Acta,

652 75(13), 3815–3838, doi:10.1016/j.gca.2011.04.011, 2011.

653 Hetényi, G., Cattin, R., Brunet, F., Bollinger, L., Vergne, J., Nábělek, J. L. and Diament, M.: Density

654 distribution of the India plate beneath the Tibetan plateau: Geophysical and petrological constraints on

655 the kinetics of lower-crustal eclogitization, Earth Planet. Sci. Lett., 264(1–2), 226–244,

656 doi:10.1016/j.epsl.2007.09.036, 2007.

657 Hodges, K. V., Hurtado, J. M. and Whipple, K. X.: Southward extrusion of Tibetan crust and its effect

658 on Himalayan tectonics, Tectonics, 20(6), 799–809, doi:10.1029/2001TC001281, 2001.

659 Holland, T. J. B., Redfern, S. A. T. and Pawley, A. R.: Volume behavior of hydrous minerals at high

660 pressure and temperature; II, Compressibilities of lawsonite, zoisite, clinzozoisite, and epidote, Am.

661 Mineral., 81(3–4), 341–348, doi:10.2138/am-1996-3-408, 1996.

662 Holland, T. J. B. and Powel, R.: An improved and extended internally consistent thermodynamic
663 dataset for phases of petrological interest, involving a new equation of state for solids, *J. Metamorph.*
664 *Geol.*, 29(3), 333–383, doi:10.1111/j.1525-1314.2010.00923.x, 2011.

665 Houseman, G. and McKenzie, D. P.: Numerical experiments on the onset of convective instability in
666 the Earth’s mantle, *Geophys. J. Int.*, 68(1), 133–164, doi:10.1111/j.1365-246X.1982.tb06966.x, 1982.

667 Houseman, G. A., McKenzie, D. P. and Molnar, P.: Convective instability of a thickened boundary
668 layer and its relevance for the thermal evolution of continental convergent belts, *J. Geophys. Res. Solid
669 Earth*, 86(B7), 6115–6132, doi:10.1029/JB086iB07p06115, 1981.

670 Huang, J., Tian, Z. Z., Zhang, C., Yang, J. J. and Chen, M.: Metamorphic evolution of Sumdo eclogite
671 in Lhasa Block of the Tibetan Plateau: Phase equilibrium in NCKMnFMASHTO System, *Geol. China*,
672 42(5), 1559–1571, 2015.

673 Jiang, F., Speziale, S. and Duffy, T. S.: Single-crystal elasticity of grossular- and almandine-rich
674 garnets to 11 GPa by Brillouin scattering, *J. Geophys. Res. Solid Earth*, 109(B10),
675 doi:10.1029/2004JB003081, 2004.

676 Jin, X., Zhang, Y.-X., Zhou, X.-Y., Zhang, K.-J., Li, Z.-W., Khalid, S. Bin, Hu, J.-C., Lu, L. and Sun,
677 W.-D.: Protoliths and tectonic implications of the newly discovered Triassic Baqing eclogites, central
678 Tibet: Evidence from geochemistry, Sr Nd isotopes and geochronology, *Gondwana Res.*, 69, 144–162,
679 doi:10.1016/j.gr.2018.12.011, 2019.

680 Klotz, S., Chervin, J.-C., Munsch, P. and Le Marchand, G.: Hydrostatic limits of 11 pressure
681 transmitting media, *J. Phys. D. Appl. Phys.*, 42(7), 075413, doi:10.1088/0022-3727/42/7/075413, 2009.

682 Krystopowicz, N. J. and Currie, C. A.: Crustal eclogitization and lithosphere delamination in orogens,
683 *Earth Planet. Sci. Lett.*, 361, 195–207, doi:10.1016/j.epsl.2012.09.056, 2013.

684 Levin, L. E.: Structure of the thermal lithosphere and asthenosphere beneath oceans and continents,

685 Geotectonics, 40(5), 357–366, doi:10.1134/S0016852106050037, 2006.

686 Li, B., Xu, J., Zhang, D., ZhilinYe, Huang, S., Fan, D., Zhou, W. and Xie, H.: Thermoelasticity and

687 stability of natural epidote at high pressure and high temperature: Implications for water transport

688 during cold slab subduction, Geosci. Front., (January), doi:10.1016/j.gsf.2020.05.022, 2020.

689 Li, C., van der Hilst, R. D., Meltzer, A. S. and Engdahl, E. R.: Subduction of the Indian lithosphere

690 beneath the Tibetan Plateau and Burma, Earth Planet. Sci. Lett., 274(1–2), 157–168,

691 doi:10.1016/j.epsl.2008.07.016, 2008.

692 Li, H. and Fang, J.: Crustal and upper mantle density structure beneath the qinghai-tibet plateau and

693 surrounding areas derived from EGM2008 geoid anomalies, ISPRS Int. J. Geo-Information, 6(1), 1–15,

694 doi:10.3390/ijgi6010004, 2017.

695 Li, J. X., Fan, W. M., Zhang, L. Y., Ding, L., Sun, Y. L., Peng, T. P., Cai, F. L., Guan, Q. Y. and Sein,

696 K.: Subduction of Indian continental lithosphere constrained by Eocene-Oligocene magmatism in

697 northern Myanmar, Lithos, 348–349, 105211, doi:10.1016/j.lithos.2019.105211, 2019.

698 Li, Z.-H., Liu, M. and Gerya, T.: Lithosphere delamination in continental collisional orogens: A

699 systematic numerical study, J. Geophys. Res. Solid Earth, 121(7), 5186–5211,

700 doi:10.1002/2016JB013106, 2016.

701 Liu, H., Xiao, Y., Van den Kerkhof, A., Wang, Y., Zeng, L. and Guo, H.: Metamorphism and fluid

702 evolution of the Sumdo eclogite, Tibet: Constraints from mineral chemistry, fluid inclusions and

703 oxygen isotopes, J. Asian Earth Sci., 172(September 2018), 292–307, doi:10.1016/j.jseaes.2018.09.013,

704 2019.

705 Liu, Y., Santosh, M., Yuan, T., Li, H. and Li, T.: Reduction of buried oxidized oceanic crust during

706 subduction, *Gondwana Res.*, 32, 11–23, doi:10.1016/j.gr.2015.02.014, 2016.

707 Lu, C., Mao, Z., Lin, J., Zhuravlev, K. K., Tkachev, S. N. and Prakapenka, V. B.: Elasticity of single-

708 crystal iron-bearing pyrope up to 20 GPa and 750 K, *Earth Planet. Sci. Lett.*, 361, 134–142,

709 doi:10.1016/j.epsl.2012.11.041, 2013.

710 Ma, L., Wang, B.-D., Jiang, Z.-Q., Wang, Q., Li, Z.-X., Wyman, D. A., Zhao, S.-R., Yang, J.-H., Gou,

711 G.-N. and Guo, H.-F.: Petrogenesis of the Early Eocene adakitic rocks in the Napuri area, southern

712 Lhasa: Partial melting of thickened lower crust during slab break-off and implications for crustal

713 thickening in southern Tibet, *Lithos*, 196–197, 321–338, doi:10.1016/j.lithos.2014.02.011, 2014.

714 Matchette-Downes, H., van der Hilst, R. D., Gilligan, A. and Priestley, K.: Seismological constraints

715 on the density, thickness and temperature of the lithospheric mantle in southwestern Tibet, *Earth Planet.*

716 *Sci. Lett.*, 524, 115719, doi:10.1016/j.epsl.2019.115719, 2019.

717 Meng, Y., Weidner, D. J. and Fei, Y.: Deviatoric stress in a quasi-hydrostatic diamond anvil cell:

718 Effect on the volume-based pressure calibration, *Geophys. Res. Lett.*, 20(12), 1147–1150,

719 doi:10.1029/93GL01400, 1993.

720 Milani, S., Nestola, F., Alvaro, M., Pasqual, D., Mazzucchelli, M. L., Domeneghetti, M. C. and Geiger,

721 C. A.: Diamond–garnet geobarometry: The role of garnet compressibility and expansivity, *Lithos*, 227,

722 140–147, doi:10.1016/j.lithos.2015.03.017, 2015.

723 Milani, S., Angel, R. J., Scandolo, L., Mazzucchelli, M. L., Ballaran, T. B., Klemme, S., Domeneghetti,

724 M. C., Miletich, R., Scheidl, K. S., Derzsi, M., Tokár, K., Prencipe, M., Alvaro, M. and Nestola, F.:

725 Thermo-elastic behavior of grossular garnet at high pressures and temperatures, *Am. Mineral.*, 102(4),

726 851–859, doi:10.2138/am-2017-5855, 2017.

727 Miller, C., Schuster, R., Klotzli, U., Frank, W. and Purtscheller, F.: Post-Collisional Potassic and

728 Ultrapotassic Magmatism in SW Tibet: Geochemical and Sr-Nd-Pb-O Isotopic Constraints for Mantle

729 Source Characteristics and Petrogenesis, *J. Petrol.*, 40(9), 1399–1424, doi:10.1093/petroj/40.9.1399,

730 1999.

731 Morency, C.: Numerical simulations of the mantle lithosphere delamination, *J. Geophys. Res.*, 109(B3),

732 B03410, doi:10.1029/2003JB002414, 2004.

733 Nábělek, P. I. and Nábělek, J. L.: Thermal characteristics of the Main Himalaya Thrust and the Indian

734 lower crust with implications for crustal rheology and partial melting in the Himalaya orogen, *Earth*

735 *Planet. Sci. Lett.*, 395, 116–123, doi:10.1016/j.epsl.2014.03.026, 2014.

736 Nishihara, Y., Takahashi, E., Matsukage, K. and Kikegawa, T.: Thermal equation of state of omphacite,

737 *Am. Mineral.*, 88(1), 80–86, doi:10.2138/am-2003-0110, 2003.

738 Nomade, S., Renne, P. R., Mo, X., Zhao, Z. and Zhou, S.: Miocene volcanism in the Lhasa block, Tibet:

739 spatial trends and geodynamic implications☆, *Earth Planet. Sci. Lett.*, 221(1–4), 227–243,

740 doi:10.1016/S0012-821X(04)00072-X, 2004.

741 Pandolfo, F., Nestola, F., Cámera, F. and Domeneghetti, M. C.: High-pressure behavior of space group

742 P2/n omphacite, *Am. Mineral.*, 97(2–3), 407–414, doi:10.2138/am.2012.3928, 2012a.

743 Pandolfo, F., Nestola, F., Cámera, F. and Domeneghetti, M. C.: New thermoelastic parameters of

744 natural C2/c omphacite, *Phys. Chem. Miner.*, 39(4), 295–304, doi:10.1007/s00269-012-0484-1, 2012b.

745 Panza, G. F., Brandmayr, E. and Romanelli, F.: A geophysical perspective on the lithosphere–

746 asthenosphere system from Periadriatic to the Himalayan areas: the contribution of gravimetry, *Rend.*

747 *Lincei*, 31(0123456789), 59–67, doi:10.1007/s12210-020-00892-z, 2020.

748 Pavese, A., Diella, V., Pischedda, V., Merli, M., Bocchio, R. and Mezouar, M.: Pressure-volume–

749 temperature equation of state of andradite and grossular, by high-pressure and -temperature powder

750 diffraction, *Phys. Chem. Miner.*, 28(4), 242–248, doi:10.1007/s002690000144, 2001.

751 Peng, M., Jiang, M., Li, Z.-H., Xu, Z., Zhu, L., Chan, W., Chen, Y., Wang, Y., Yu, C., Lei, J., Zhang,

752 L., Li, Q. and Xu, L.: Complex Indian subduction style with slab fragmentation beneath the Eastern

753 Himalayan Syntaxis revealed by teleseismic P-wave tomography, *Tectonophysics*, 667, 77–86,

754 doi:10.1016/j.tecto.2015.11.012, 2016.

755 Qin, F., Wu, X., Wang, Y., Fan, D., Qin, S., Yang, K., Townsend, J. P. and Jacobsen, S. D.: High-

756 pressure behavior of natural single-crystal epidote and clinozoisite up to 40 GPa, *Phys. Chem. Miner.*,

757 43(9), 649–659, doi:10.1007/s00269-016-0824-7, 2016.

758 Ren, Y. and Shen, Y.: Finite frequency tomography in southeastern Tibet: Evidence for the causal

759 relationship between mantle lithosphere delamination and the north–south trending rifts, *J. Geophys.*

760 *Res.*, 113(B10), B10316, doi:10.1029/2008JB005615, 2008.

761 Rivers, M., Prakapenka, V., Kubo, A., Pullins, C., Holl, C. and Jacobsen, S.: The

762 COMPRES/GSECARS gas-loading system for diamond anvil cells at the Advanced Photon Source,

763 *High Press. Res.*, 28(3), 273–292, doi:10.1080/08957950802333593, 2008.

764 Robertson, E. C.: Thermal properties of rocks., 1988.

765 Schulte-Pelkum, V., Monsalve, G., Sheehan, A., Pandey, M. R., Sapkota, S., Bilham, R. and Wu, F.:

766 Imaging the Indian subcontinent beneath the Himalaya, *Nature*, 435(7046), 1222–1225,

767 doi:10.1038/nature03678, 2005.

768 Semprich, J., Simon, N. S. C. and Podladchikov, Y. Y.: Density variations in the thickened crust as a

769 function of pressure, temperature, and composition, *Int. J. Earth Sci.*, 99(7), 1487–1510,

770 doi:10.1007/s00531-010-0557-7, 2010.

771 Shi, D., Zhao, W., Klemperer, S. L., Wu, Z., Mechie, J., Shi, J., Xue, G. and Su, H.: West–east

772 transition from underplating to steep subduction in the India–Tibet collision zone revealed by receiver-
773 function profiles, *Earth Planet. Sci. Lett.*, 452, 171–177, doi:10.1016/j.epsl.2016.07.051, 2016.

774 Shi, D., Klemperer, S. L., Shi, J., Wu, Z. and Zhao, W.: Localized foundering of Indian lower crust in
775 the India-Tibet collision zone, *Proc. Natl. Acad. Sci. U. S. A.*, 117(40), 24742–24747,
776 doi:10.1073/pnas.2000015117, 2020a.

777 Shi, Y.-N., Niu, F., Li, Z.-H. and Huangfu, P.: Craton destruction links to the interaction between
778 subduction and mid-lithospheric discontinuity: Implications for the eastern North China Craton,
779 *Gondwana Res.*, 83, 49–62, doi:10.1016/j.gr.2020.01.016, 2020b.

780 Singh, A. and Kumar, M. R.: Seismic signatures of detached lithospheric fragments in the mantle
781 beneath eastern Himalaya and southern Tibet, *Earth Planet. Sci. Lett.*, 288(1–2), 279–290,
782 doi:10.1016/j.epsl.2009.09.031, 2009.

783 Singh, H. and Mahatsente, R.: Lithospheric Structure of Eastern Tibetan Plateau from Terrestrial and
784 Satellite Gravity Data Modeling: Implication for Asthenospheric Underplating, edited by S. Roeske,
785 *Lithosphere*, 2020(1), doi:10.2113/2020/8897964, 2020.

786 Skinner, B. J.: Section 6: Thermal expansion, in *Handbook of Physical Constants*, pp. 75–96,
787 Geological Society of America., 1966.

788 Tang, Y., Qin, Y., Gong, X., Duan, Y., Chen, G., Yao, H., Liao, J., Liao, S., Wang, D. and Wang, B.:
789 Discovery of eclogites in Jinsha River suture zone, Gonjo County, eastern Tibet and its restriction on
790 Paleo-Tethyan evolution, *China Geol.*, 3(1), 83–103, doi:10.31035/cg2020003, 2020.

791 Turner, S., Hawkesworth, C., Liu, J., Rogers, N., Kelley, S. and van Calsteren, P.: Timing of Tibetan
792 uplift constrained by analysis of volcanic rocks, *Nature*, 364(6432), 50–54, doi:10.1038/364050a0,
793 1993.

794 Wang, C., Zhao, X., Liu, Z., Lippert, P. C., Graham, S. A., Coe, R. S., Yi, H., Zhu, L., Liu, S. and Li,
795 Y.: Constraints on the early uplift history of the Tibetan Plateau, *Proc. Natl. Acad. Sci.*, 105(13), 4987–
796 4992, doi:10.1073/pnas.0703595105, 2008.

797 Wang, C., Chen, W.-P. and Wang, L.-P.: Temperature beneath Tibet, *Earth Planet. Sci. Lett.*, 375, 326–
798 337, doi:10.1016/j.epsl.2013.05.052, 2013.

799 Wang, Q., Wyman, D.A., Li, Z.X., Sun, W., Chung, S.L., Vasconcelos, P.M., Zhang, Q.Y., Dong, H.,
800 Yu, Y.S., Pearson, N., Qiu, H.N., Zhu, T.X.: Eocene north–south trending dikes in central Tibet: new
801 constraints on the timing of east. *Earth and Planetary Science Letters* 298 (1–2), 205–21,
802 doi:10.1016/j.epsl.2010.07.046, 2010.

803 Wang, X., Holt, W. E. and Ghosh, A.: Joint modeling of lithosphere and mantle dynamics: Sensitivity
804 to viscosities within the lithosphere, asthenosphere, transition zone, and D“ layers, *Phys. Earth Planet.
805 Inter.*, 293(March), 106263, doi:10.1016/j.pepi.2019.05.006, 2019.

806 Wittlinger, G., Farra, V., Hetényi, G., Vergne, J. and Nábělek, J.: Seismic velocities in Southern Tibet
807 lower crust: a receiver function approach for eclogite detection, *Geophys. J. Int.*, 177(3), 1037–1049,
808 doi:10.1111/j.1365-246X.2008.04084.x, 2009.

809 Xu, J., Zhang, D., Dera, P., Zhang, B. and Fan, D.: Experimental evidence for the survival of augite to
810 transition zone depths, and implications for subduction zone dynamics, *Am. Mineral.*, 102(7), 1516–
811 1524, doi:10.2138/am-2017-5959, 2017.

812 Xu, J., Zhang, D., Fan, D., Zhang, J. S., Hu, Y., Guo, X., Dera, P. and Zhou, W.: Phase Transitions in
813 Orthoenstatite and Subduction Zone Dynamics: Effects of Water and Transition Metal Ions, *J. Geophys.
814 Res. Solid Earth*, 123(4), 2723–2737, doi:10.1002/2017JB015169, 2018.

815 Xu, J., Zhang, D., Fan, D., Dera, P. K., Shi, F. and Zhou, W.: Thermoelastic Properties of Eclogitic

816 Garnets and Omphacites: Implications for Deep Subduction of Oceanic Crust and Density Anomalies

817 in the Upper Mantle, *Geophys. Res. Lett.*, 46(1), 179–188, doi:10.1029/2018GL081170, 2019.

818 Xu, J., Fan, D., Zhang, D., Li, B., Zhou, W. and Dera, P. K.: Investigation of the crystal structure of

819 low water content hydrous olivine to 29.9 GPa: a high-pressure single-crystal X-ray diffraction study,

820 *Am. Mineral.*, doi:10.2138/am-2020-7444, 2020a.

821 Xu, J., Fan, D., Zhang, D., Guo, X., Zhou, W. and Dera, P. K.: Phase Transition of Enstatite-Ferrosilite

822 Solid Solutions at High Pressure and High Temperature: Constraints on Metastable Orthopyroxene in

823 Cold Subduction, *Geophys. Res. Lett.*, 47(12), 1–10, doi:10.1029/2020GL087363, 2020b.

824 Yang, J., Xu, Z., Li, Z., Xu, X., Li, T., Ren, Y., Li, H., Chen, S. and Robinson, P. T.: Discovery of an

825 eclogite belt in the Lhasa block, Tibet: A new border for Paleo-Tethys?, *J. Asian Earth Sci.*, 34(1), 76–

826 89, doi:10.1016/j.jseae.2008.04.001, 2009.

827 Yang, Y., Abart, R., Yang, X., Shang, Y., Ntaflos, T. and Xu, B.: Seismic anisotropy in the Tibetan

828 lithosphere inferred from mantle xenoliths, *Earth Planet. Sci. Lett.*, 515, 260–270,

829 doi:10.1016/j.epsl.2019.03.027, 2019.

830 Ye, Z., Fan, D., Tang, Q., Xu, J., Zhang, D. and Zhou, W.: Constraining the density evolution during

831 destruction of the lithospheric mantle in the eastern North China Craton, *Gondwana Res.*, 91, 18–30,

832 doi:10.1016/j.gr.2020.12.001, 2021.

833 Zhai, Q., Zhang, R., Jahn, B., Li, C., Song, S. and Wang, J.: Triassic eclogites from central Qiangtang,

834 northern Tibet, China: Petrology, geochronology and metamorphic P–T path, *Lithos*, 125(1–2), 173–

835 189, doi:10.1016/j.lithos.2011.02.004, 2011a.

836 Zhai, Q., Jahn, B., Zhang, R., Wang, J. and Su, L.: Triassic Subduction of the Paleo-Tethys in northern

837 Tibet, China: Evidence from the geochemical and isotopic characteristics of eclogites and blueschists

838 of the Qiangtang Block, *J. Asian Earth Sci.*, 42(6), 1356–1370, doi:10.1016/j.jseaes.2011.07.023,

839 2011b.

840 Zhang, D., Hu, Y. and Dera, P. K.: Compressional behavior of omphacite to 47 GPa, *Phys. Chem.*

841 *Miner.*, 43(10), 707–715, doi:10.1007/s00269-016-0827-4, 2016.

842 Zhang, D., Dera, P. K., Eng, P. J., Stubbs, J. E., Zhang, J. S., Prakapenka, V. B. and Rivers, M. L.:

843 High Pressure Single Crystal Diffraction at PX², *J. Vis. Exp.*, 2017(119), 1–9, doi:10.3791/54660,

844 2017a.

845 Zhao, M.-S., Chen, Y.-X. and Zheng, Y.-F.: Geochemical evidence for forearc metasomatism of

846 peridotite in the Xigaze ophiolite during subduction initiation in Neo-Tethyan Ocean, south to Tibet,

847 *Lithos*, 380–381, 105896, doi:10.1016/j.lithos.2020.105896, 2021.

848 Zhu, D.-C., Wang, Q., Zhao, Z.-D., Chung, S.-L., Cawood, P. A., Niu, Y., Liu, S.-A., Wu, F.-Y. and

849 Mo, X.-X.: Magmatic record of India-Asia collision, *Sci. Rep.*, 5(1), 14289, doi:10.1038/srep14289,

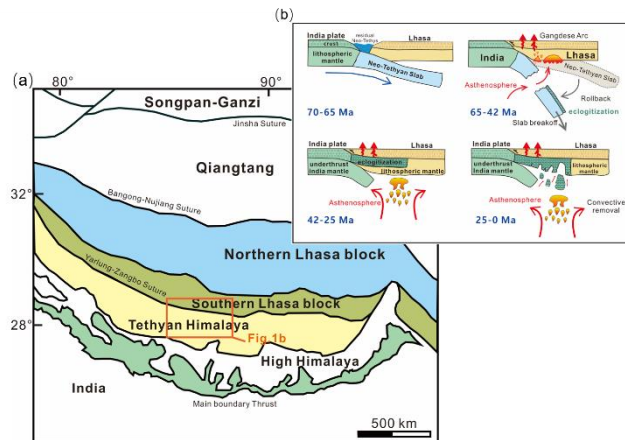
850 2015.

851 Zou, Y., Gréaux, S., Irifune, T., Whitaker, M. L., Shinmei, T. and Higo, Y.: Thermal equation of state

852 of Mg₃Al₂Si₃O₁₂ pyrope garnet up to 19 GPa and 1700 K, *Phys. Chem. Miner.*, 39(7), 589–598,

853 doi:10.1007/s00269-012-0514-z, 2012.

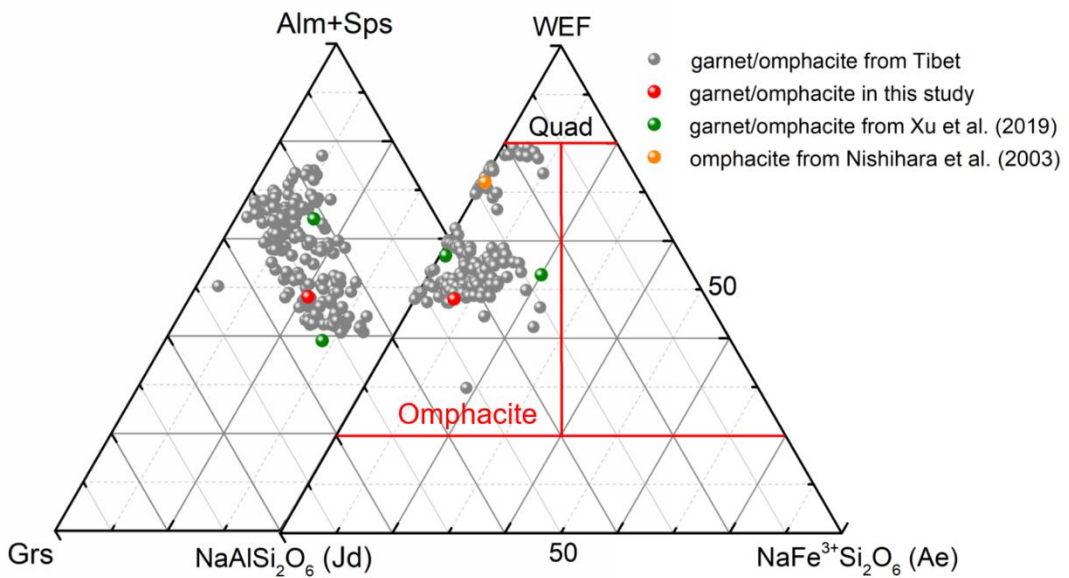
854 **Figure:**



855

856 **Figure 1.** (a) Schematic geological map of the Tibetan Plateau (modified from Chung et al. 2005
857 and Wang et al. 2010). (b) Interpretive geological cartoon of India-Asia collision evolution. 70-65
858 Ma: The flat Neo-Tethyan oceanic slab subducts beneath Tibet with the closure of the Neo-Tethys
859 Ocean. 65-42 Ma: The rollback of the Neo-Tethyan slab breaks off after densification by
860 eclogitization. 42-25 Ma: The subduction of the Indian continent continued at a low subduction
861 angle beneath the Lhasa terrane and was accompanied by heavy thermal perturbation. 25-0 Ma:
862 The thickened eclogitic lower crust undergoes the “convective removal” of delamination due to
863 gravitational instability.

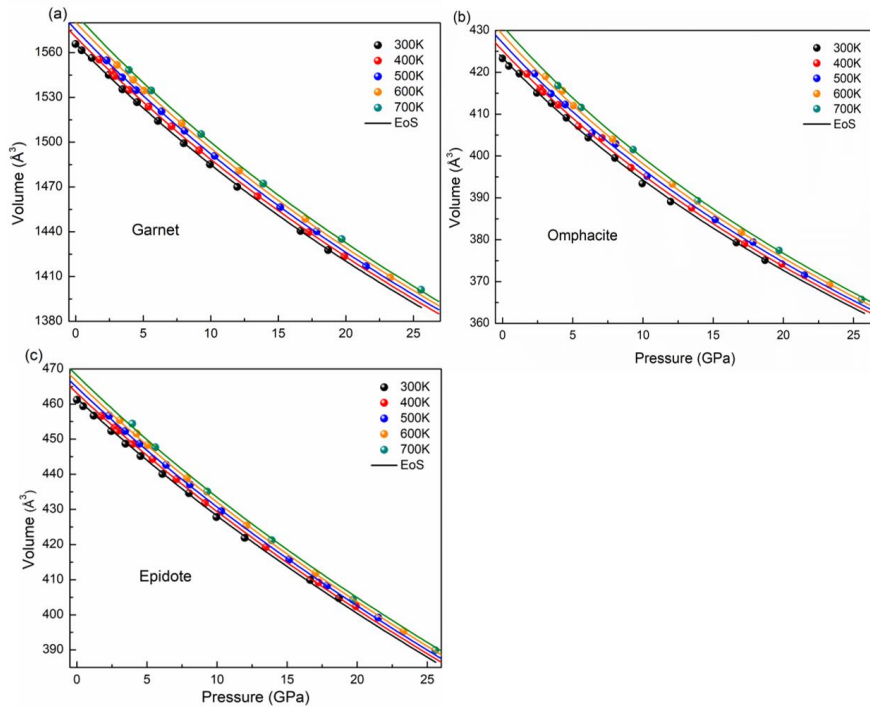
864



865

866 **Figure 2.** Composition of garnet and omphacite in eclogites from Tibet and this study. The gray
 867 solid circles represent the components of garnet and omphacite collected from previous studies in
 868 Tibet (e.g. Chan et al., 2009; Liu et al., 2019; Song et al., 2003; Weller et al., 2016; Yang et al.,
 869 2009; Zhai et al., 2011a). The green solid circles are garnet and omphacite with different Fe
 870 contents according to Xu et al. (2019). The orange solid circles are omphacite according to
 871 Nishihara et al. (2003). The red solid circles are the components of garnet and omphacite in this
 872 study. Prp = pyrope, Alm = almandine, Grs = grossular, Sps = spessartine, Quad = Ferrosilite +
 873 enstatite + wollastonite, Jd = jadeite, and Ae = aegirine.

874

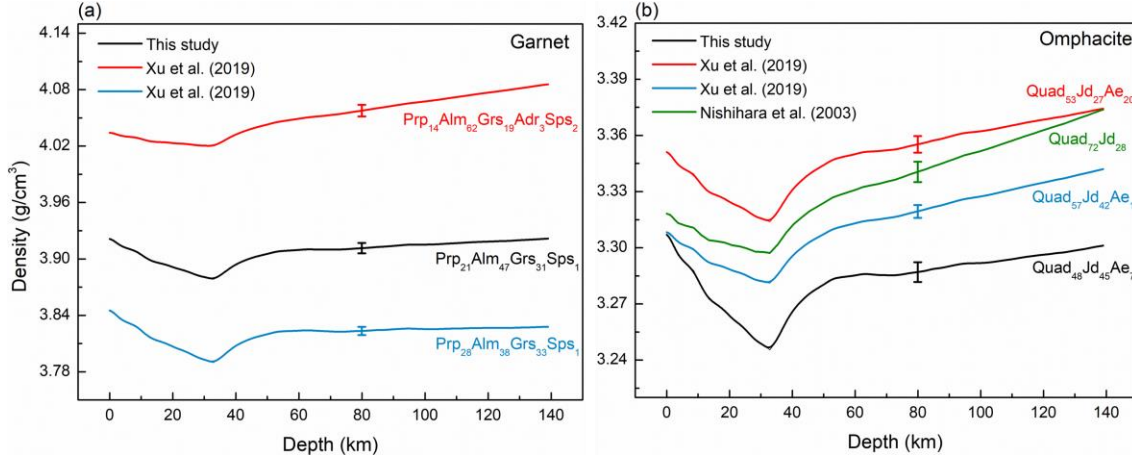


875

876 **Figure 3.** Pressure-volume-temperature relations of garnet (a), omphacite (b), and epidote (c).

877 Isothermal compression curves are calculated by using the thermoelastic parameters obtained in

878 this study.



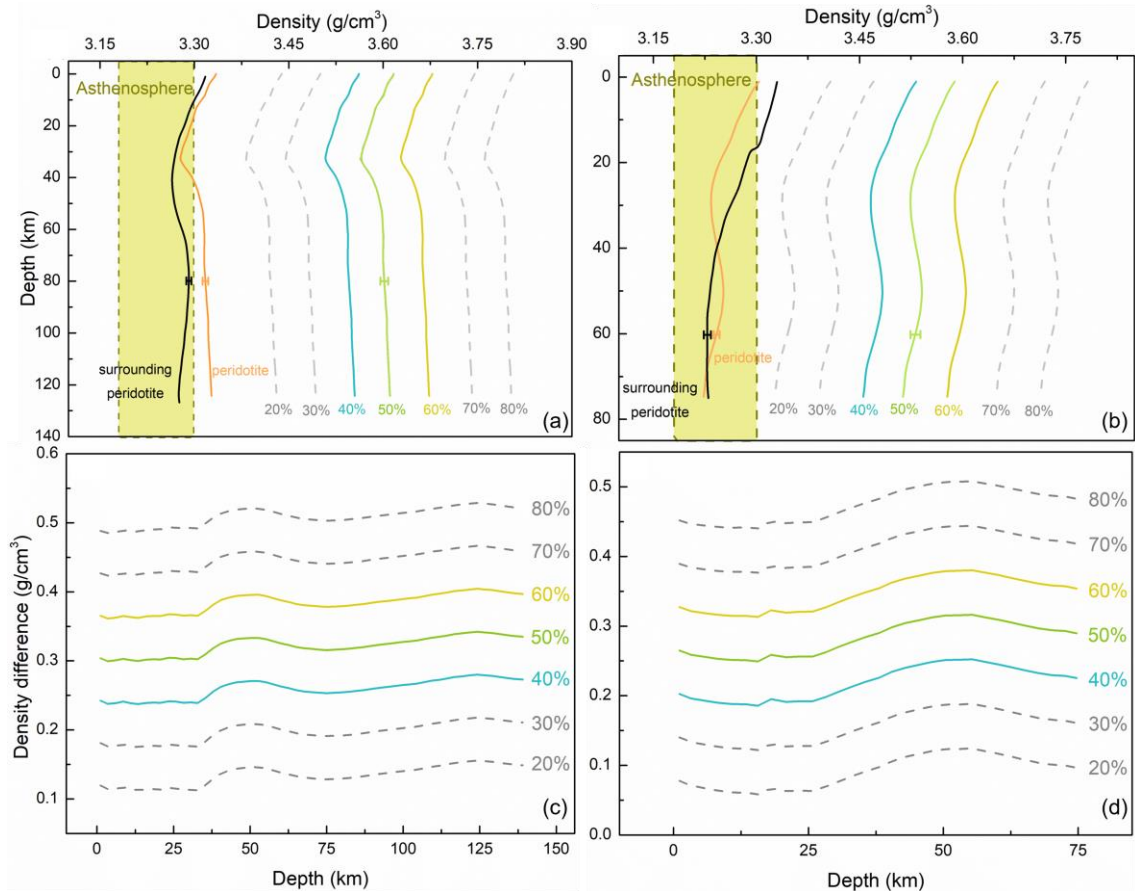
879

880 **Figure 4.** Density profiles of garnet (a) and omphacite (b) along with the cold Tibetan geothermal

881 line (Wang et al., 2013). The garnets of $\text{Prp}_{21}\text{Alm}_{47}\text{Grs}_{31}\text{Sps}_1$ and $\text{Prp}_{28}\text{Alm}_{38}\text{Grs}_{33}\text{Sps}_1$ are from

882 Xu et al. (2019). The omphacites of $\text{Quad}_{53}\text{Jd}_{27}\text{Ae}_{20}$ and $\text{Quad}_{57}\text{Jd}_{42}\text{Ae}_1$ are from Xu et al. (2019)

883 and $\text{Quad}_{72}\text{Jd}_{28}$ is from Nishihara et al. (2003).

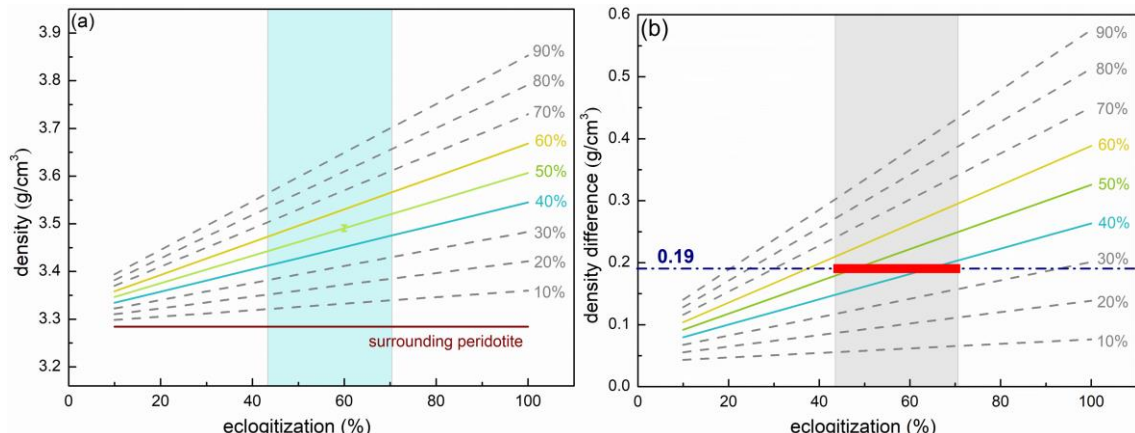


884

885 **Figure 5.** Density profiles of eclogite and peridotite assemblages ((a) and (b)) and density
 886 difference between eclogite and peridotite ((c) and (d)) in Tibet along the Paleozoic and Cenozoic
 887 geothermal lines under the conditions of Neo-Tethyan oceanic slab detachment (a) (Wang et al.,
 888 2013) and subduction of the Indian continental margin beneath the Lhasa terrane (b) (Craig et al.,
 889 2020). The percentage represents the content of garnet in eclogite, of which epidote accounts for 5
 890 vol. % by default. The orange curve and black curve show the density profile of peridotite with a
 891 composition of 70 vol. % olivine + 25 vol. % orthopyroxene + 3 vol. % clinopyroxene + 2 vol. %
 892 spinel. The orange line shows the density of peridotite in the lithospheric mantle along the
 893 Paleozoic (a) (Wang et al., 2013) and Cenozoic (b) (Craig et al., 2020) geothermal lines, and the
 894 black curve indicates that the density of peridotite in the surrounding lithospheric mantle is along
 895 the Paleozoic (a) (Nábělek and Nábělek, 2014) and Cenozoic (b) (Wang et al., 2013) geothermal

896 lines in Tibet. The shaded region is the density range of the asthenosphere (Chen and Tenzer, 2019;
897 Levin, 2006; Panza et al., 2020; Singh and Mahatsente, 2020).

898



899
900 **Figure 6.** (a) The effect of eclogitization on the density of the subducted slab at ~80 km (2.6 GPa
901 and 625 °C) along the Paleozoic geothermal line. The percentage on the right represents the
902 content of garnet and the content of epidote is fixed at 5 vol. % by default. The content of garnets
903 in Tibet is between 40 vol. % and 60 vol. %. The density represents the average density of the
904 subducted slab with the entire eclogitic ocean lower crust and partially eclogitized lithospheric
905 mantle, where the degree of eclogitization refers to the lithospheric mantle. The rufous line
906 represents the average density of surrounding peridotite in this study. The blue shading indicates
907 the possible degree of eclogitization. (b) Density difference between eclogite with different
908 degrees of eclogitization and surrounding peridotite. The red dashed solid line represents a density
909 excess of 0.19 g/cm³ from the isostatic balance and the geoid anomaly (Matchette-Downes et al.,
910 2019).
911